Strain Induced Material Nonlinearity for AGARD Wing 445.6 in a Virtual Wind Tunnel Environment: Results from Coupled Multiphysics Simulation.

CMS Group*
Code 6304
U.S. Naval Research Laboratory
Washington DC, 20375
* Composite Materials and Structures Group:
J. Michopoulos, R. Badaliance, T. Chwastyk, L. Gause, P. Mast

C. Farhat, M. Lessoine
Center for Aerospace Structures
Dept. of Aerospace Engineering Sciences
University of Colorado at Boulder
Boulder, CO 80309-0429

Abstract

This project used parallel solvers with coupled fluid-structure interaction to predict the energy absorption and material softening distributions on a wing structure, for various angles of attack and far field Mach numbers. The structural solution was computed on the geometry of the AGARD 445.6 wing for the case of a polymer matrix composite (PMC), with a local measure of softening damage based on nonlinear constitutive behavior determined from experiment. Hot zones of incipient softening were observed to shift unexpectedly with angle of attack and Mach number.

The coupled system of partial differential equations governing the behavior of the wing was solved using Finite Element Tear and Interconnect (FETI) methods along with implicit and explicit time marching techniques. Comparison of code results to experimental data indicated high efficiency and accuracy. The fluid model was decomposed to four sub-domains and its explicit integration was distributed to four CPUs of an Origin 2000, while the structural model was not decomposed and was implemented on a fifth CPU.

NRL's PMC characterization of the softening behavior is achieved by automated materials testing, and by following a systems identification approach that yields a constitutive relationship. The constitutive relationship leads to a local measure of damage (Dissipated Energy Density) given local strains. Applying this measure to strains based on undamaged material showed where the onset of damage could be expected; this location shifted as fluid parameters varied.

Introduction

The two main drivers for the work represented in the present document are:

- the enormous technology pull of the evolving computational technology, automation of symbolic mathematics and program synthesis,
- the need-based application push for realistic systemic prediction/simulation, inexpensive material qualification-certification, quick material insertion, and rapid prototyping and production, of Navy structures.

Virtual Prototyping and Design (VPD) as an upcoming discipline combining technology, automation, modeling tools and domain expert knowledge utilization, attempts to respond to these drivers.

VPD of composite structures, under realistic loads, imposed from the fluid-structure linear and non-linear interaction, are of paramount importance to the cost and mission efficiency. It is anticipated, that structures designed through the utilization of virtual wind tunnel (VWT), technologies along with inherently accurate composite material characterization, will have a direct and high impact on the manufacturing precision and demanding tolerances required for increased Precision Force capability.

In addition, the success of designing PMC Navy structures within mission and economic requirements depends highly on the accuracy of the predictive capability of the structural and fluid models used. This in turn depends on two major issues:

- The loads on the structure are not definable apriori , but rather a consequence of the structure's interaction with the fluid around it as a function of the operational requirements of the mission envelope description (i.e. mach numbers, altitudes, maneuverability constrains etc)
- The accurate model for the constitutive response of the material used to design the structure at hand under multiple loading paths.

The Data Driven Design Workbench (D^3W) is a an object oriented distributed computational environment under development at NRL, that allows the user to succesfully address these issues for PMC structures. The first issue has been recently addressed in collaboration with the University of Colorado at Boulder via the addition of coupled fluid-structure modeling and analysis modules to the D^3W. The second issue has been addressed through accurate material behavior modeling based on data from computationally controlled massive experimentation for the sake of material behavior identification.

An brief description of the methodology and the integration of these two approaches is given below.

The purpose of the present paper is to demonstrate how the usage of such an environment can expose levels of behavioral detail that cannot be anticipated without exercising models that account for the fluid-structure interaction coupling and the actual softening behavior of the material.

Virtual Wind Tunnel Implementation

Coupled Aeroelastic Fluid-Structure Modelling

In order to predict the dynamic response of a rigid or flexible structure in a fluid flow, the equations of motion of the structure and the fluid must be solved simultaneously to account for the actual coupling between the two continua. The most difficult part of handling the fluid/structure coupling numerically stems from the fact that the structural equations are usually written with material (Lagrangian) coordinates, while the fluid equations are typically written using spatial (Eulerian) coordinates. Therefore, a straightforward approach to the solution of the coupled fluid/structure dynamic equations requires moving at each time step at least the portions of the fluid grid that are close to the moving structure. This can be acceptable for small displacements of the structure, but may lead to severe grid distortions when the structure undergoes large motion. Recently, several different approaches have emerged as an alternative to partial regridding in transient aeroelastic computations. Among these the most noteworthy are the corotational approach [1,2], dynamic meshes [3], and the Arbitrary Lagrangian Eulerian (ALE) [4] formulation.

The moving mesh can be modeled [5] as an independent field with its own dynamics. Therefore, the coupled transient aeroelastic problem can be formulated as a three-field rather than two-field coupled problem: the fluid, the structure and the dynamic mesh, in the form of the following semi discrete PDEs

$$\frac{\partial}{\partial t}(A(x,t)W(x,t)) + \tilde{F}_c^c(W((x,t),x,\dot{x})) = \tilde{F}^d(W(x,t)) \quad (1a)$$

$$M\frac{\partial^2}{\partial t^2}u + f^{\text{int}}(u) = f^{ext}(W(x,t)) \quad (1b)$$

$$\tilde{M}\frac{\partial^2}{\partial t^2}x + \tilde{D}\frac{\partial}{\partial t}x + \tilde{K}_c x = K_c u(W(x,t)) \quad (1c)$$

where: W is the fluid state vector, A results from the finite element/volume discretization of the fluid equations, $\tilde{F}_c^c$ is the convected vector of numerical convective fluxes, $\tilde{F}^d$ is the vector of numerical diffusive fluxes, u is the structural displacement vector, f^{int} is the vector of internal forces on the structure, f^{ext} is the vector of external forces on the structure, M is the finite element mass matrix of the structure, $\tilde{M}$ and $\tilde{D}$, and $\tilde{K}$ are fictitious mass, damping and stiffness matrices associated with the fluid moving grid and constructed to avoid parasitic interaction between the fluid and its grid, or the structure and the moving fluid.

Solution Procedures

Heterogeneous time integration procedures for fully-coupled transient computations require "time marching" through a combination of staggering and subcycling procedures [6]. The opportunity for implementing the fluid and structural solvers on multiple processors of different computers in a heterogeneous environment suggests a staggering procedure where both disciplines are advanced in parallel. This enhances the speed of the simulation by allowing interparallel processing on top of the intraparallel computations; the speed comes at the expense of a deterioration in accuracy, especially in the structure solution. However, this trade-off of accuracy for speed may be desirable in a preliminary design.

At every time step, the corresponding linearized system of equations is solved via the FETI (Finite Element Tearing and Interconnecting) substructuring method [7,8]. The FETI algorithm is an optimal domain decomposition iterative algorithm which is based on a saddle point variational principle. It incorporates a mechanically sound preconditioner and a natural coarse grid operator that propagate the error globally, accelerate convergence, and ensure performance independent of mesh size and number of substructures. Hence, the FETI method is well suited for massively parallel implicit computations.

The massively parallel viscous flow solver used is based on a mixed finite volume/finite element formulation [9]. An ALE formulation is incorporated in this fluid solver to obtain the benefits previously described.

The computational approach outlined above requires the explicit prediction of the motion of the fluid grid points on the fluid/structure interface once the motion of the structure has been determined, and the transmission of the pressure loads from the fluid side of that interface to the structural nodes that lie on it.

The fluid and structure meshes have two independent representations of the physical fluid/structure interface. This creates the problem that the fluid and structure interfaces are not identical, and their discretizations do not coincide.

These issues have been addressed through MATCHER, a parallel software module that generates the data structures needed for handling arbitrary and nonconforming fluid/structure interfaces in transient aeroelastic computations.

Automated Characterization of PMCs

In order to characterize the constitutive response of a PMC system, NRL has developed a system identification approach utilizing custom made testing machines that exposes material specimens to discrete loading paths spanning the loading space of the specimen structure. Two characteristic examples of such machines are the In Plane Loader System (IPLS) and the Six Degree of freedom Loader System (6DLS) shown in figure 1a and 1b respectively. Details about these machines and the associated automated processes are given extensively in [10-12].

Specimen Considerations

Composite materials associated with various applications range through a wide variety of materials. Each different combination of matrix, fiber, fiber coating (for matrix-fiber interphase), layup angle, stacking sequence, etc. corresponds to a dif-ferent material. The approach discussed here is specifically tailored to PMCs. Approximately 100 material systems with fibers ranging from Kevlar to IM7 graphite and several thermoset resins and thermoplastic organic polymers have been tested and characterized with the approach dis-cussed here. A partial list of all the materials tested up to now can be found in [11].

The specimen geometry was designed to satisfy the following requirements:

- The characteristic dimensions should be large enough relative to fiber diam-eter and lamina thickness to ensure that the material could be analyzed as ei-ther a single mechanically equivalent homogeneous anisotropic monolithic material, or a collection of layers of varying orientations of such materials.
- The overall specimen size should be small enough to keep material costs at a manageable level.
- Strain riser(s) should be present to guarantee that high strain regions occur well away from all specimen boundaries.

Procedure

The objective of the IPLS is to control the rigid body motion of the boundary of the specimen that is held by the movable grip and at the same time measure the boundary displacements and tractions. Because the actuators are constrained to move in a plane parallel to the specimen, the resulting motion involves only three degrees of freedom relative to any frame of reference on that plane. The grip motion can be resolved into three basic components: sliding (shearing) u_0, opening/closing u_1, and rotation u_2. Specified combinations of actuator displacements, therefore, map into particular combinations of these three basic motions.

In order to visualize the loading space it is advantageous to think in terms of a three dimensional displacement space with coordinates (u_0, u_1, u_2). The issue then is how to select a representative family of paths that cover the space and how to sample along each path. It was decided to cover the boundary displacement space with a set of 15 uniformly distributed radial loading paths as indicated in Fig. 2. Note that because of geometry and material symmetry about the axis along the notch(es), only the half space corresponding to positive sliding displacement ($u_0>0$) need be considered. The required set of observation points is generated by sampling along each path. A particular test in which the actuator

motions are continuously varied corresponds to a specific path in this space. Only 15 specimens are required, and 50 observations per loading path are obtained from a single specimen.

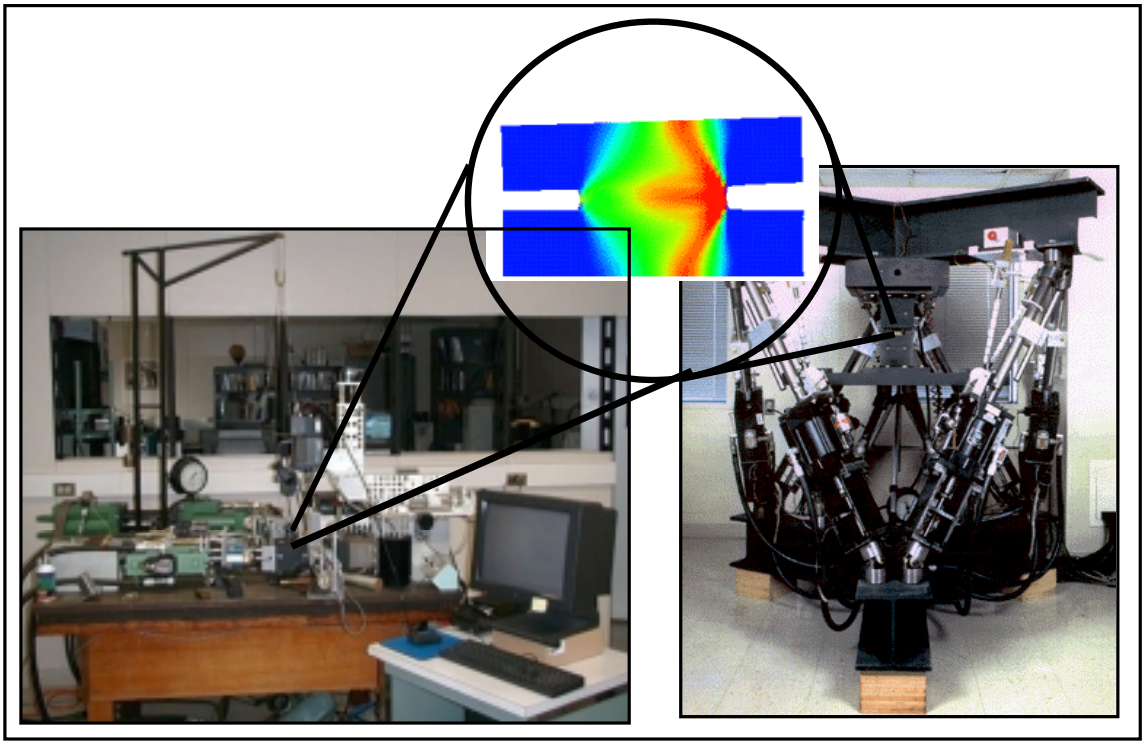

Figure 1. Views of IPLS (left) and the 6DLS (right) along with an indicative specimen view (top center) of the associated dissipated energy density.

The locus of the end points of all loading paths for the same increment is a sphere as shown in Fig. 2, where two arbitraty loading paths at three arbitrary increments are presented as an example along with the two basis case loading paths of pure shearing, and opening.

The spatial distributions of dissipated energy density after the dssipated energy density function has been determined via the process described below, are shown in Fig. 2 at three specific points on its one of the loading paths.

The process of computing the total dissipated energy is based on the boundary displacements and tractions that are measured at each increment imposed by the IPLS along each loading path. More details are presented elsewhere [11-14]. One specimen per loading path is used initially and the procedure is then repeated for a total of two specimens per loading path.

The dissipated energy density function is constructed as a sum of basis functions χ_i that depend only on the local strain state $\tilde{\varepsilon}$ of the material in the structure, and are weighted by coefficients c_i that depend only on the material:

$$\phi(\tilde{\varepsilon},m)=\phi(\tilde{\varepsilon},\tilde{c})=c_1(m)\chi_1(\tilde{\varepsilon})+c_2(m)\chi_2(\tilde{\varepsilon})+\ldots+c_n(m)\chi_n(\tilde{\varepsilon}) \qquad (2)$$

This particular form for ϕ , accomplises a full decomposition of the effects of the geometry from those of the material by forcing it to be only a function of the strain state. It also, accomplishes scale independence within the domain of application of the continuum hypothesis.

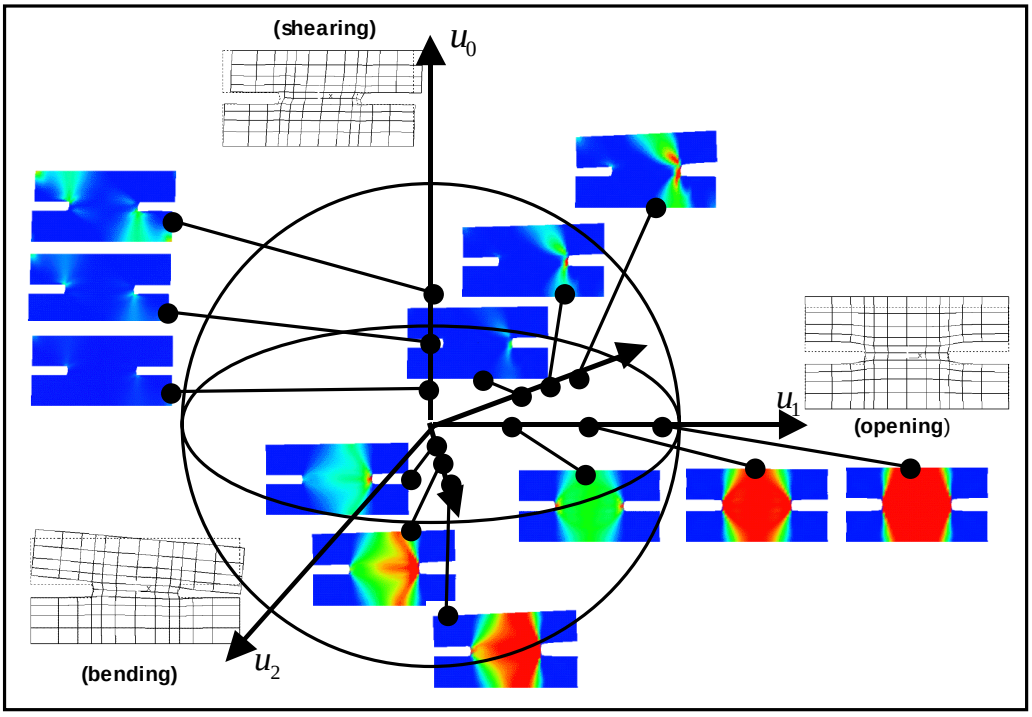

Figure 2. In plane loading space and associated loading paths along with post computes distributions of dissipated energy density of specimens at corresponding points of the loading paths shown.

Determination of the dissipated energy density function can be accomplished by employing a desirable vector space defining the polynomials representing the basis functions, and subsequently determine the coefficients c_i. This is accopmplished by considering the energy balance equation,

$$\int_0^{u_r} t_u q_v dq^v - \frac{1}{2} t_s u_t u^v = \int_{\partial V} \phi(\varepsilon_i(x_j)) dx_j \qquad (3)$$

The left had side represents the dissipated energy lost in the structure as the difference between the total energy imparted by the testing machine to the specimen, minus the recoverable energy. Where *t* and *u* are used to name the components of the boundary tractions and displacements respectively.

The right hand side of Eq. (3) represent the dissipated energy list in the structure as the integral over the volume of the specimen of the dissipated energy density function.

The discrete form of this equation -resulting from consideration of the total energy as the sum of energies for each finite element of the model for the specimen-, can be written for as many times as needed in order to define an overdetermined system of linear equations with c_i as uknowns. Since this system is overdetermined, and since we have to consider the monotonicity and positive definitiveness of ϕ, the problem can be considered to be a global optimization problem with inequality constrains. Various algorithms are available to use for solving this problem. We have been using random hill climb with reversal algorithm as it has been captured in the ACM TOMS library algorithm 587 [15].

The D^3W simulation environment

The Architecture

Figure 3 shows the block diagram of D^3W's main components and their relationship in terms of data flow paths. This diagram is intended to represent its abstract architecture. The main components of the environment and a short description of their function are described below.

- ***Fluid-Structural Analysis:*** This module consists of structural analysis codes. For the case of traditional structures commercial codes like ANSYS are used. For the case of wing or other shell-like structures interacting with fluids two parallelized codes that have been custom developed at the University of Colorado at Boulder are used. These codes accept fluid properties, flight conditions, and structural properties and they can compute any fluid or structure related field results.
- ***Base Case Solutions:*** This module is a database that stores all basis case strain field solutions that the user generates through the Fluid-Structural Analysis module for the structure involved.
- ***Load Space Controller:*** This module defines the loading vector space and its bases and produces parametric representations of desired loading paths applied onto the structure via explicit loading conditions, or implicit ones via loading event parameterization.
- ***Material Space Controller:*** This module defines the material properties vector space and its bases and produces parametric representations of desired material change paths applied onto the structure via explicit laminate selection conditions, or implicit ones via constituent (resin and fiber) property parameterization.

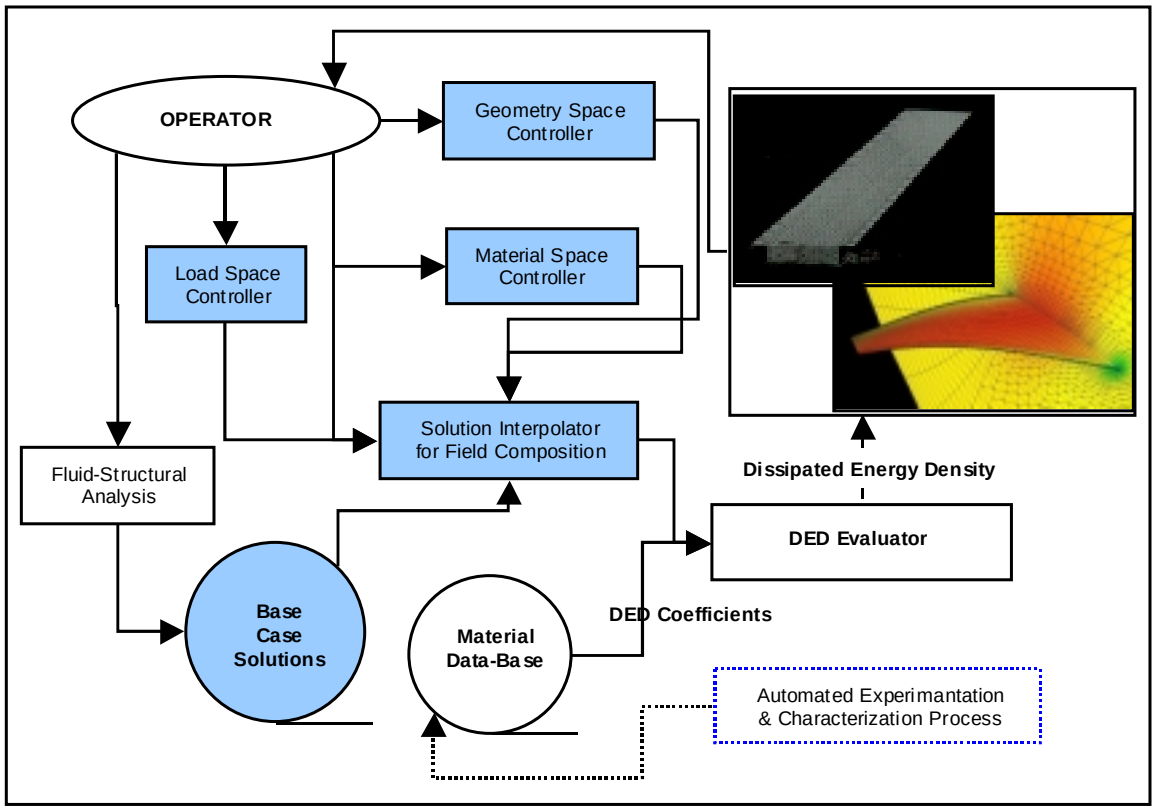

Figure 3. Architecture of the Data Driven Design Workbench

- ***Geometry Space Controller:*** This module defines the geometrical features vector space and its bases and produces parametric representations of desired feature change paths applied onto the structure via explicit geometry altering conditions.
- ***Material Database:*** This module contains the values of all the coefficients identified to define a dissipated energy density function suitable to represent the constitutive response of various material systems.
- ***Solution Interpolator:*** This module combines all the selections from the controllers for loading, material and geometry path definitions, and synthesizes from the base case solutions database, the desired combined solution.
- ***DED Evaluator:*** This module utilizes the output strain field of the solution interpolator module and with the help of material database computes the scalar distribution of dissipated energy for every point in the structure.
- ***Display Module:*** The user interaction and visualization module.

This architecture has evolved through time and the whole environment along with the DED methodology have been utilized in various applications including health prediction and sensor optimization of smart structures [16-18].

Code Validation

The AGARD 445.6 wing was selected as the representative structure for code validation because of the fact that there exist actual wind tunnel data associated with its performance [19,20]. A consequence of the experimental data has been that it has been used as a benchmark case for various analytical and numerical modeling techniques which are also available in the literature [21].

The first AGARD standard aeroelastic configuration for dynamic response, Wing 445.6 [19], was tested in the 16–foot Transonic Dynamics Tunnel (TDT) at the NASA Langley Research Center [20]. The wing had a quarter-chord sweep angle of 45^{o}, a panel aspect ratio of 1.65, a taper ratio of 0.66, and a NACA 65A004 airfoil section. Several models of the wing were tested in the TDT including full span and semi-span models. The model used in this study is a semi-span, wall-mounted model that was constructed of laminated mahogany. The root chord of this model was 1.833 feet and the semi-span was 2.5 feet. In order to obtain flutter data for a wide range of Mach number and density conditions in the TDT, holes were drilled through the mahogany wing to reduce its stiffness. Filling these holes with rigid foam plastic preserved the aerodynamic shape of the original wing. Flutter data for this model -tested in air- are reported in Ref. [20] over a range of Mach number from 0.338 to 1.141. Natural boundary-layer transition was allowed throughout the test. The semi-span model was attached directly to the wind tunnel wall (no splitter plate was used); therefore, the wing root was immersed in the wall boundary layer. Ref. [19] indicates that the displacement thickness of the wall boundary layer was 0.8 inch or less.

Figure 4 shows a comparison of the evolution of the flutter speed index as a function of the far field mach number, from the experimental data [20], and two modeling approaches [3,21] that integrate the Navier-Stokes equations, as well the present approach. Clearly, in the region below mach 0.93 our approach demonstrated the best performance both in terms of computational resources (grid points and explicit integration time step length), as well as closeness to the experimental data.

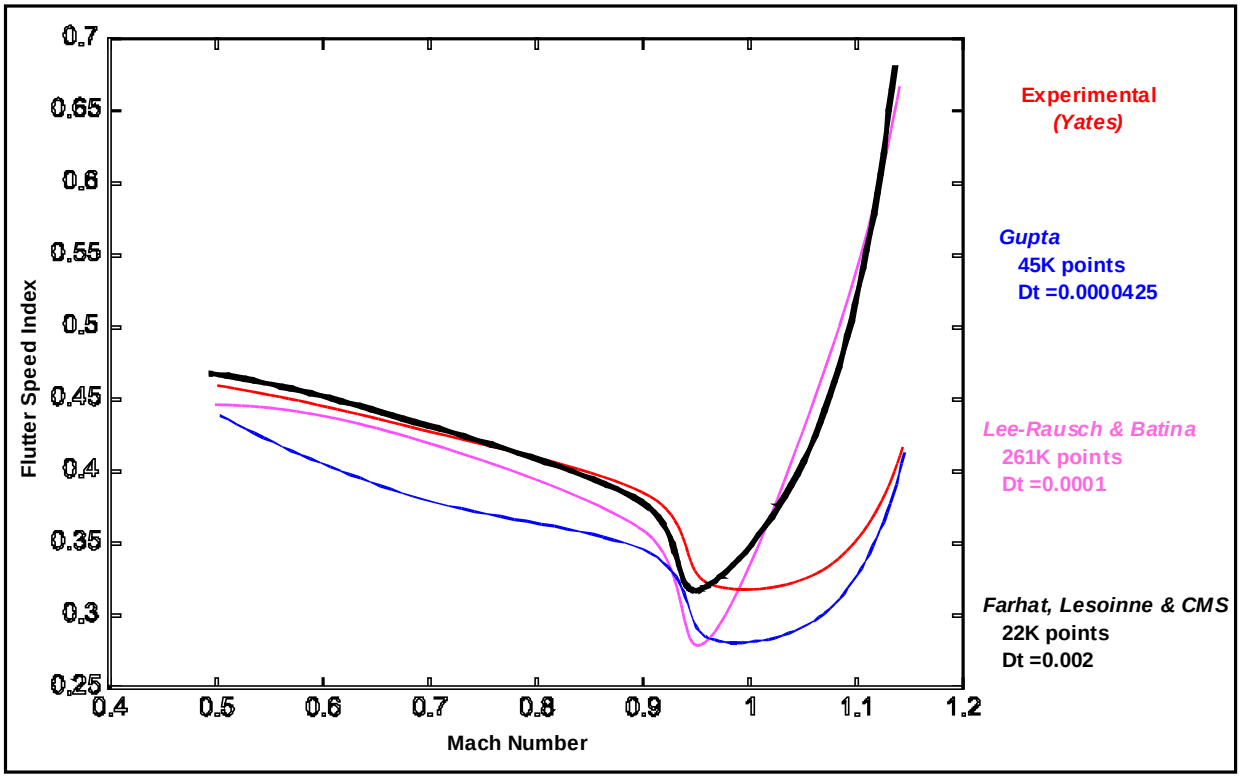

Figure 4. Distribution of Flutter Speed Index vs. far field Mach number from experimental and various numerical simulations results.

Simulation Results

Subsonic linear unsteady aerodynamics and solution algorithms have been reasonably successful in predicting flutter boundaries for Mach numbers up to 0.6 or 0.7. However, linear theory has been unable to account for the effects upon transient loads of aerodynamic shape, high angles of attack, detaching and reattaching flows, moderate to low dynamic pressure, or maneuvering conditions [22].

In an attempt to account for material nonlinear behavior due to strain induced damage, NRL's D^3W has been extended to solve coupled fluid/structure problems. The AGARD 445.6 wing was modeled and an analysis was performed to obtain strain fields which were used to compute dissipated energy density for each loading condition that is defined by a specific combination of angle of attack and far field mach number.

Our results from the AGARD 445.6 wing are based a model of 462 nodes and 800 triangular element mesh for the structure, and a mesh of 38491 nodes and 218156 tetrahedral elements for the fluid. The fluid was decomposed in four domains while the structure was used as one domain. All solutions ran on 5 processors of NRL's *Origin 2000* system. This problem ran in approximately 10 minutes per loading condition. However, most of the time was consumed to generate the multiple results files that included the nodal values of the fluid speed and pressure, as well as the strain and stress components for the upper lower and middle sections of the shell elements used to model the structure of the wing.

Figure 5 shows a typical distribution of the steady state solutions for the fluid speed (Fig. 5a.x) and pressure (Fig. 5b.x) on the boundary of the fluid formed by the bottom of the wing, for the case of

far field mach $M_\infty = 0.9$ and for angle of attack α, at 0^o (Figs. 5a.1, 5b.1) and 9^o (Figs. 5a.2, 5b.2). These results are consistent with the ones published in Refs. [19-21]. A characteristic of these results is that for the case of $M_\infty = 0.9$ and $\alpha = 9°$ the highest pressure area (yellow) has shifted towards the trailing edge of the wing (Fig. 5b.2).

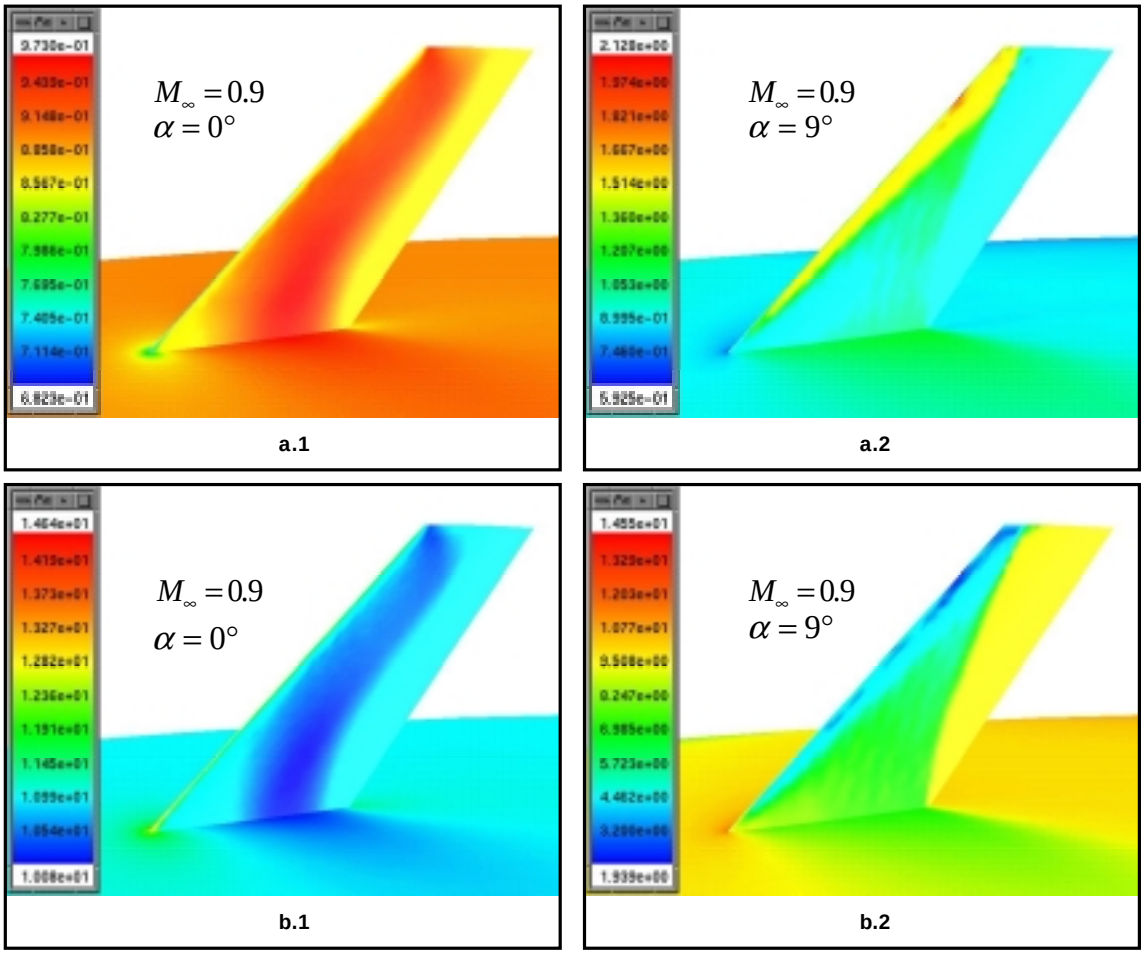

Figure 5. Mach number (top) and pressure (bottom) distributions on the bottom side of the wing for M = 0.9 and angle of attack 0 (column 1) and 9 (column 2) degrees.

Figure 6 shows the distributions of dissipated energy density as a measure of the onset of nonlinear behavior of the composite material selected to construct the wing for the parametric region bounded by $0.5 \le M_\infty \le 0.9$ and $0° \le \alpha \le 9°$.

As expected the highest angle of attack with the highest far field fluid speed generates the most critical loading condition in terms of total softening on the structure. The most critical observation from these results is evidenced from the cases for angles of attack higher that 7^o where it appears that there is a shifting of the hot zone from the basis of the wing to the leading edge as the fluid speed increases.

A more detailed view of this phenomenon appears in Fig. 7 which shows the variation of the dissipated energy density distributions on the wing for $M_\infty = 0.5$ and angle of attack varying from $\alpha = 0°$ through $\alpha = 9°$ plotted in relative color scale in order to accentuate the differences within each loading case. This case reveals multiple shifting of the hot zone for local material softening.

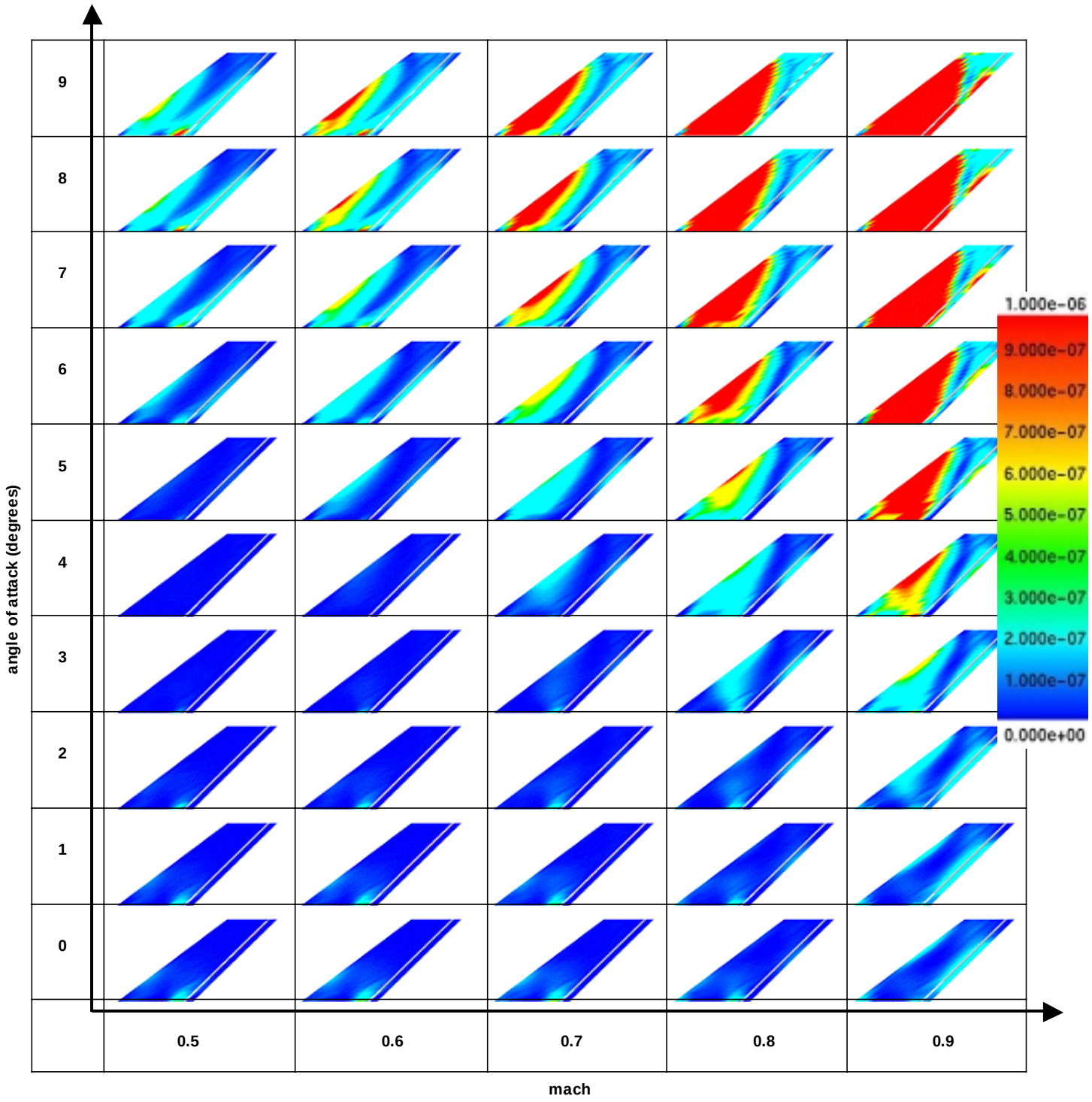

Figure 6. Distribution of strain induced dissipated energy density for various loading conditions defined by specific far field Mach number and angle of attack.

It originaly starts at the root of the wing near the trailing edge, then shifts to the middle of the leading edge and the middle of trailing edge and finally it returns back to the root of the wing with a secondary zone developing at the leading edge near the root of the wing.

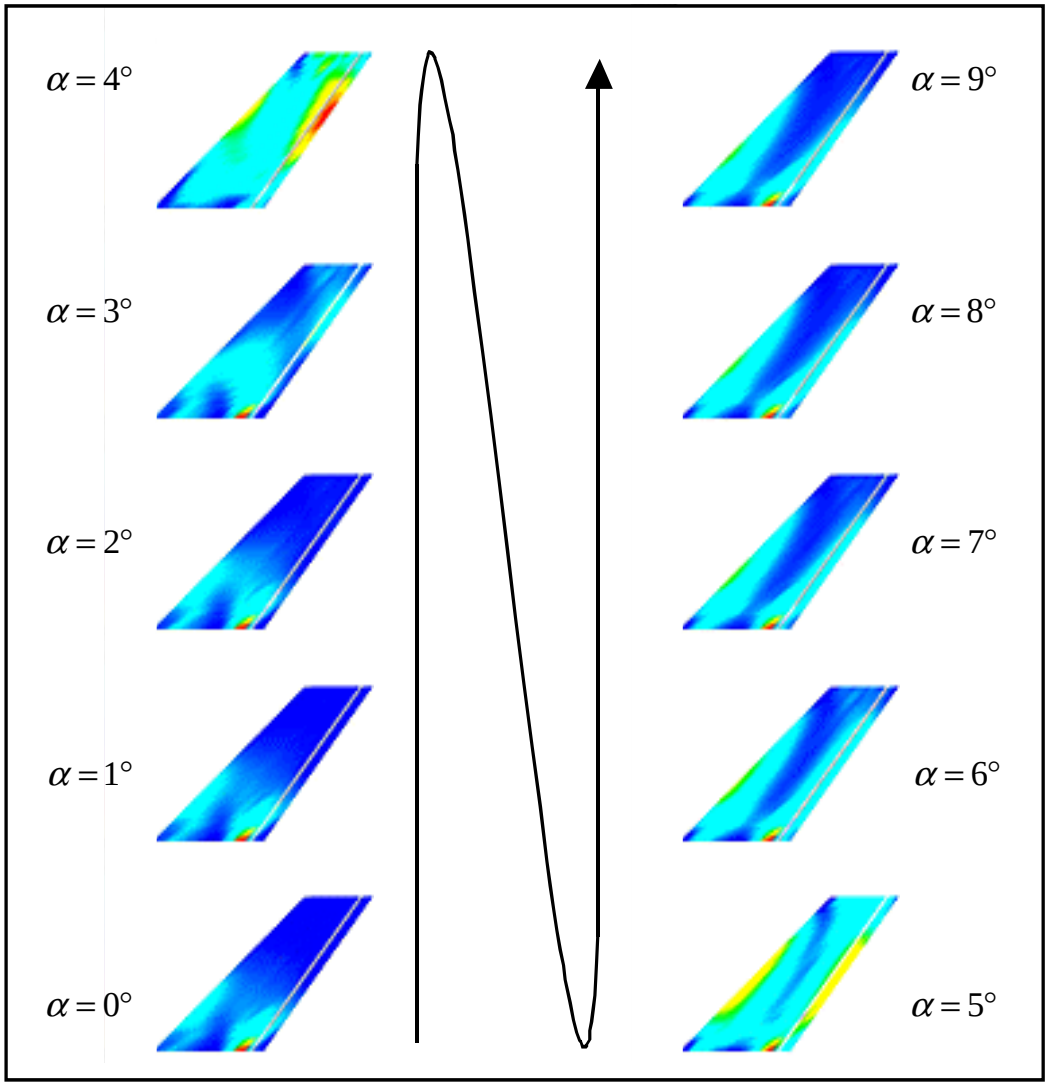

Figure 7. Distribution of dissipated energy density as a function of increasing angle of attck for far field Mach number 0.5

This behavior expands the premise of ultimate scalar quantities (such as material strength) as being sufficient for the structural design process. Dissipated energy density distribution as a measure of local material softening clearly demonstrates positional shifting and therefore it introduces the concept of loading space dimensionality and loading path direction as important additional factors besides load magnitude in the structural design discipline.

Figure 8 shows the distributions of dissipated energy density in relative color scale, as a function of the mach number M_∞ for angles of attack $\alpha = 0°$ and $\alpha = 9°$. Here it is evident again that the hot spot shifting effect is taking place again as a function of the far field fluid speed. In the case of angle of attack $\alpha = 9°$ the shefting occures from the root of the wing near the trailing edge to the leading edge and then back to the root.

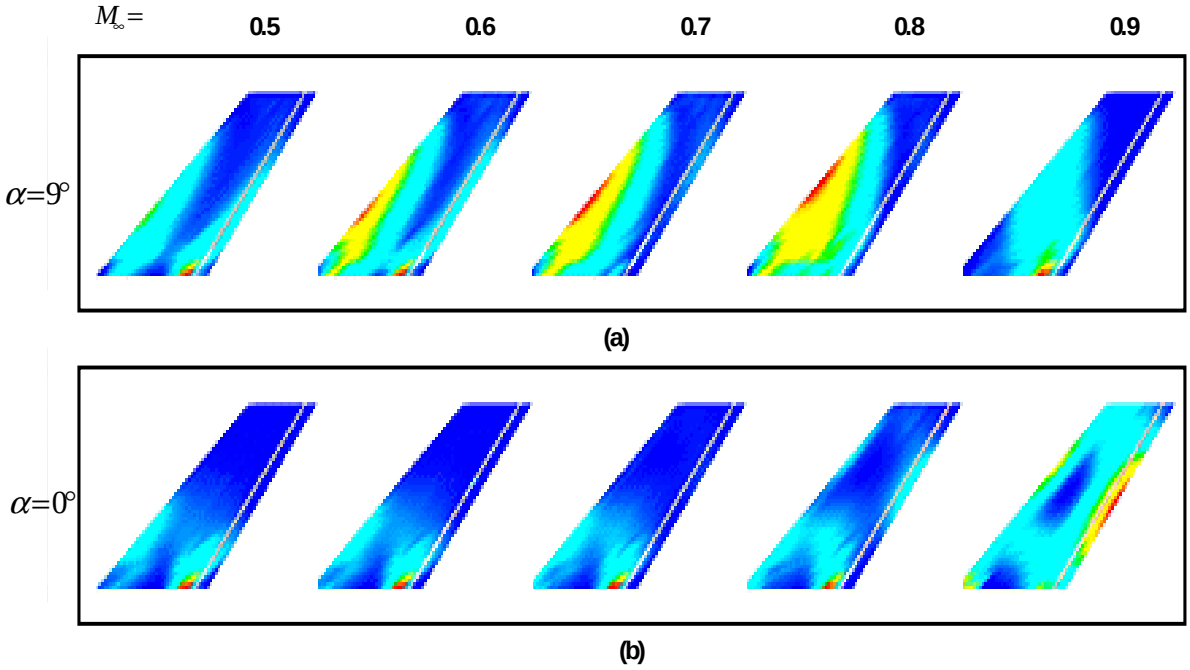

Figure 8. Distributions of dissipated energy density as a function of increasing far field Mach number, for angles of attack 9 (a) and 0 (b) degrees.

For the case of $\alpha = 0°$ the shifting occurs from the root of the wing near the trailing edge to bothe the leading and the trailing edges at about half the wing span.

Acknowledgments

The authors would like Dr. H. Dardy Chief Scientist for Advanced Computing of NRL's Center for Computational Sciences, for his support and help in facilitating the logistics for accessing the NRL clusters from the early days.

References

[1] O. A. Kandil and H. A. Chuang, Unsteady Vortex-Dominated Flows Around Maneuvering Wings Over a Wide Range of Mach Numbers, *AIAA 26th Aerospace Sciences Meeting*, (AIAA Paper No. 88-0317, 1988).

[2] C. Farhat and T. Y. Lin, Transient Aeroelastic Computations Using Multiple Moving Frames of Reference, *AIAA 8th Applied Aerodynamics Conference*, (AIAA Paper No. 90-3053, 1990).

[3] J. T. Batina, Unsteady Euler Airfoil Solutions Using Unstructured Dynamic Meshes, *AIAA 27th Aerospace Sciences Meeting*, (AIAA Paper No. 89- 0115, 1989).

[4] J. Donea, An Arbitrary Lagrangian-Eulerian Finite Element Method for Transient Fluid-Structure Interactions, *Comp. Meth. Appl. Mech. Engng.*, 33, 689-723, 1982.

[5] C. Farhat, M. Lesoinne, P. Chen and S. Lanteri, Parallel heterogeneous Algorithms for the Solution of Three-Dimensional Transient Coupled Aeroelastic Problems, *AIAA/ASME/ASCE/AHS/ASC Structures, Structural Dynamics and Materials Conference*, AIAA Paper No. 95-1290, 1146-1160, (1995).

[6] C. Farhat, Finite Element Heterogeneous Algorithms for Transient Aeroelastic Computations, *Second Japan-US Symposium on Finite Element Methods for Fluid Dynamics*, (1994).

[7] C. Farhat and F. X. Roux, A Method of Finite Element Tearing and Interconnecting and its Parallel Solution Algorithm, *International Journal for Numerical Methods in Engineering*, 32,1205-1227, (1991).

[8] C. Farhat and M. Lesoinne, Automatic Partitioning of Unstructured Meshes for the Parallel Solution of Problems in Computational Mechanics, *International Journal for Numerical Methods in Engineering*, 36, 745-764, (1993).

[9] C. Farhat, L. Fezoui, and S. Lanteri, Two-Dimensional Viscous FlowComputations on the Connection Machine: Unstructured Meshes, UpwindSchemes, and Massively Parallel Computations, *Computer Methods in Applied Mechanics and Engineering*, 102, 61-88, (1993).

[10] P.W. Mast, L.A. Beaubien, M. Clifford, D.R. Mulville, S.A Sutton., R. Thomas, J. Tirosh, and I. Wolock, A semi-automated in-plane loader for material testing, *Experimental Mechanics*, 32,. 236-241,(1983).

[11] P.W. Mast, G.E. Nash, J.G. Michopoulos, R.W. Thomas, R. Badaliance, and I. Wolock, *Experimental determination of dissipated energy density as a measure of strain-induced damage in composites*, Technical Report NRL/FR/6383--92-9369, (Naval Research Laboratory, Washington, DC.,1992).

[12] P.W. Mast, J.G. Michopoulos, R.W. Thomas, R. Badaliance, I. Wolock, Characterization of strain-induced damage in composites based on the dissipated energy density: Part I - Basic scheme and formulation, *Int. Jnl. of Theor. and Applied Fract. Mech.*, 22, 71-96,(1995).

[13] P.W. Mast, J.G. Michopoulos, R.W. Thomas, R. Badaliance, I. Wolock, Characterization of strain-induced damage in composites based on the dissipated energy density: Part II - Composite specimens and naval structures, *Int. Jnl. of Theor. and Applied Fract. Mech.*, 22, 97-114, (1995).

[14] P.W. Mast, J.G. Michopoulos, R.W. Thomas, R. Badaliance, I. Wolock, Characterization of strain-induced damage in composites based on the dissipated energy density: Part III -General material constitutive relation, *Int. Jnl. of Theor. and Applied Fract. Mech.*, 22, 115-125, (1995).

[15] R. J. Hanson and K. H. Haskell, Algorithm 587, *ACM-Trans. Math. Software*, 8, No. 3, 323, (1982).

[16] J.G. Michopoulos, P.W. Mast, R. Badaliance, I. Wolock, Health Monitoring of smart structures by the use of dissipated energy, ASME proc. 93 WAM on *Adaptive structures and material systems*, G.P. Carman/E. Garcia,eds., (ASME, AD-Vol. 35, 1993) 457-462.

[17] P. W. Mast, J.G. Michopoulos, R. Badaliance, H. Chaskelis, Dissipated energy as the means for health monitoring of smart structures, *SPIE Proc. Smart Structures and Materials 1994, Smart Sensing, Processing, and Instrumentation*, J. Sirkis, ed., (SPIE, Vol. 2191, 1994) 199-207.

[18] P. R. Factory, Health error prediction and sensor topology optimization on a smart pressure vessel, *Smart Structures and Materials 1995, Industrial and Commercial Applications of Smart Structures Technologies*, (SPIE, Vol. 2447, 1995), 155-166.

[19] Yates, E. C., Jr., "AGARD Standard Aeroelastic Con-figuration for Dynamic Response, Candidate Configuration I.-Wing 445.6," NASA TM 100492, August 1987.

[20] Yates, E. C., Jr.; Land, N. S.; and Foughner, J. T., Jr., "Measured and Calculated Subsonic and Transonic Flutter Characteristics of a 45 deg Sweptback Wing Plaform in Air and in Freon-12 in the Langley Transonic Dynamics Tunnel," NASA TN D-1616, March 1963.

[21] E. M. Lee-Rausch, J. T. Batina, Calculation of AGARD Wing 445.6 Flutter using Navier-Stokes Aerodynamics, *AIAA 11th Applied Aerodynamics Conference*, (AIAA Paper No. 93- 3476, 1993).

[22]J. W. Edwards and J. B. Malone, Current Status of Computational Methods for Transonic Unsteady Aerodynamics and Aeroelastic Applications, *Computing Systems in Engineering*, 3, 545-569, (1992).

Figure Captions

Figure 1. Views of IPLS (left) and the 6DLS (right) along with an indicative specimen view (top center) of the associated dissipated energy density.

Figure 2. In plane loading space and associated loading paths along with post computes distributions of dissipated energy density of specimens at corresponding points of the loading paths shown.

Figure 3. Architecture of Data Driven Design Workbench.

Figure 4. Distribution of Flutter Speed Index vs. far field Mach number from experimental and various numerical simulations results.

Figure 5. Mach number (top row) and pressure (bottom row) distributions on the bottom side of the wing for M = 0.9 and angle of attack 0 (column 1) and 9 (column 2) degrees.

Figure 6. Distribution of strain induced dissipated energy density for various loading conditions defined by specific far field Mach number and angle of attack.

Figure 7. Distribution of dissipated energy density as a function of increasing angle of attack for far field Mach number 0.5

Figure 8. Distributions of dissipated energy density as a function of increasing far field Mach number, for angles of attack 9 (a) and 0 (b) degrees.